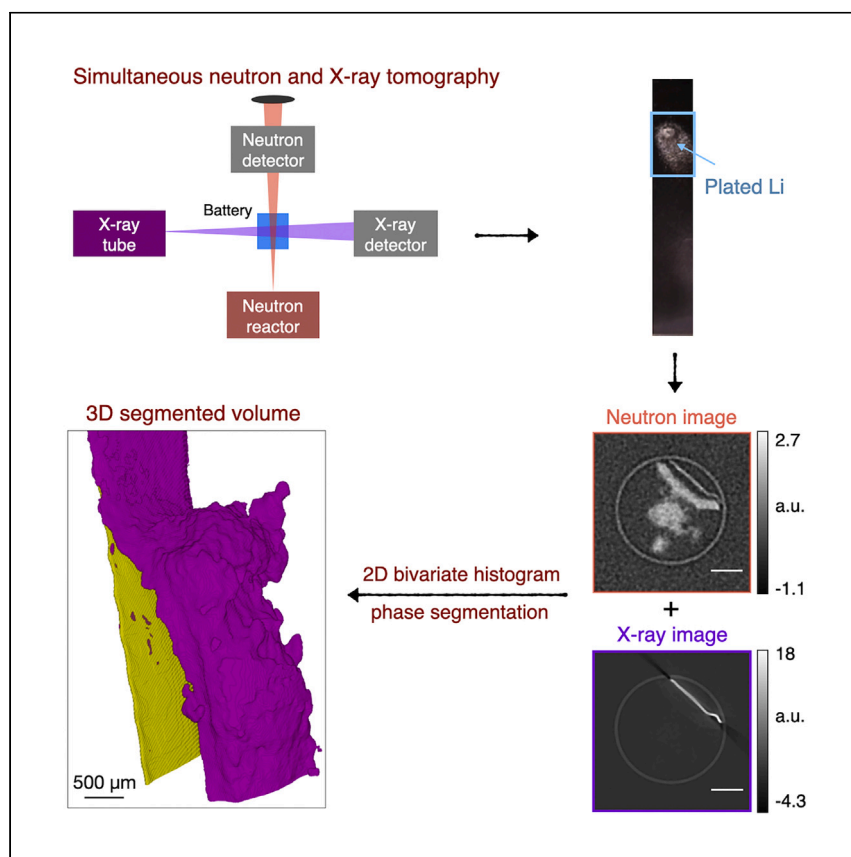## Report

Simultaneous neutron and X-ray tomography for visualization of graphite electrode degradation in fast-charged lithium-ion batteries

Maha Yusuf, Jacob M. LaManna, Partha P. Paul, ..., Hans-Georg Steinrück, Michael F. Toney, Johanna Nelson Weker

jacob.lamanna@nist.gov (J.M.L.)
michael.toney@colorado.edu (M.F.T.)
jlnelson@slac.stanford.edu (J.N.W.)

Highlights

Simultaneous neutron and X-ray tomography (NeXT) is a non-invasive imaging method

NeXT enables visualization of graphite electrode degradation after fast charging

NeXT overlaps neutron and X-ray data from same sample area to identify materials

NeXT shows qualitative correlation between electrode degradation and plated Li

Advanced battery characterization is critical to reveal fundamental degradation modes of lithium-ion batteries. Using the sensitivity of neutrons to lithium and X-rays to copper, Yusuf et al. demonstrate the viability of simultaneous neutron and X-ray tomography as a non-invasive imaging modality for visualization of graphite electrode degradation following fast charging.

Cell Reports
Physical Science

CellPress
OPEN ACCESS

Report

Simultaneous neutron and X-ray tomography for visualization of graphite electrode degradation in fast-charged lithium-ion batteries

Maha Yusuf,[1,12] Jacob M. LaManna,[2,*] Partha P. Paul,[3,4,5] David N. Agyeman-Budu,[3] Chuntian Cao,[3,6] Alison R. Dunlop,[7] Andrew N. Jansen,[7] Bryant J. Polzin,[7] Stephen E. Trask,[7] Tanvir R. Tanim,[8] Eric J. Dufek,[8] Vivek Thampy,[3] Hans-Georg Steinrück,[9] Michael F. Toney,[10,11,*] and Johanna Nelson Weker[3,13,*]

SUMMARY

Advanced battery characterization using neutron and X-ray-based imaging modalities is crucial to reveal fundamental degradation modes of lithium-ion batteries (LIBs). Taking advantage of the sensitivity of neutrons to some low-Z (Li) and X-rays to high-Z materials (Cu), here we demonstrate the viability of simultaneous neutron- and X-ray-based tomography (NeXT) as a non-destructive imaging platform for *ex situ* 3D visualization of graphite electrode degradation following extreme fast charging (XFC). In addition, we underscore the benefits of the simultaneous nature of NeXT by combining the neutron and X-ray data from the same sample location for material identification and segmentation of one pristine and two XFC-cycled graphite electrodes (9C charge for 450 cycles). Our *ex situ* results and methodology development pave the way for the design of NeXT-friendly LIB geometries that will allow operando and/or *in situ* three-dimensional (3D) visualization of electrode degradation during XFC.

INTRODUCTION

Advanced battery characterization using imaging diagnostic tools[1–6] with high spatial and/or temporal resolution is central to unravel fundamental insights about degradation mechanisms in lithium-ion batteries (LIBs). As these degradation processes span multi-length scales and multi-timescales, a combination of multiple imaging modalities is often required.[7,8] For example, although X-ray micro-computed tomography (μCT) is sensitive to Cu, it offers poor absorption contrast for low-Z elements such as Li and C at high X-ray energies that are needed to penetrate the full LIB cells. On the other hand, neutron μCT provides high sensitivity for detecting some low-Z battery materials including Li.[9]

Recently, neutron imaging has been used in conjunction with X-ray μCT to combine the advantages of both methods in correlative imaging (CI).[10–12] Because neutrons are sensitive to Li and H, and X-rays are sensitive to higher-Z Cu and Al current collectors, the combination of these two techniques enables improved understanding of the electrochemical process associated with battery degradation. Although CI is very useful, recent studies have demonstrated that collecting neutron and X-ray μCT simultaneously from the same sample location enables identification and subsequent segmentation of more components over individual segmentations of neutron and X-ray images in CI.[13,14]

[1]Department of Chemical Engineering, Stanford University, Stanford CA 94305, USA

[2]National Institute of Standards and Technology, Gaithersburg, MD 20899, USA

[3]Stanford Synchrotron Radiation Lightsource, SLAC National Accelerator Laboratory, Menlo Park, CA 94025, USA

[4]ESRF – The European Synchrotron Radiation Facility, 71 Av. des Martyrs, 38000 Grenoble, France

[5]Henry Royce Institute, Department of Materials, University of Manchester, Manchester M1 3BB, UK

[6]Computational Science Initiative, Brookhaven National Laboratory, Upton, NY 11973, USA

[7]Argonne National Laboratory, 9700 South Cass Avenue, Lemont, IL 60439, USA

[8]Idaho National Laboratory, 2525 N. Fremont, Idaho Falls, ID 83415, USA

[9]Department Chemie, Universität Paderborn, Warburger Str. 100, 33098 Paderborn, Germany

[10]Department of Chemical and Biological Engineering, University of Colorado Boulder, Boulder, CO 80309, USA

[11]Renewable and Sustainable Energy Institute, University of Colorado Boulder, Boulder, CO 80309, USA

[12]Twitter: @mahayusuf1

[13]Lead contact

*Correspondence:
jacob.lamanna@nist.gov (J.M.L.),
michael.toney@colorado.edu (M.F.T.),
jlnelson@slac.stanford.edu (J.N.W.)
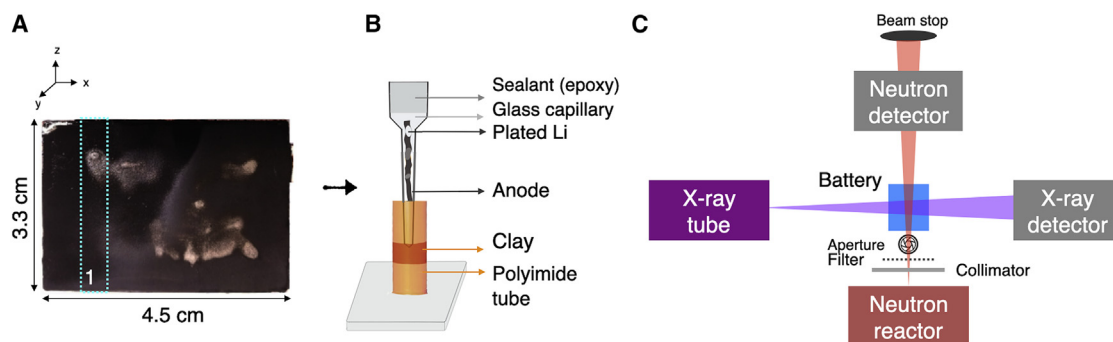https://doi.org/10.1016/j.xcrp.2022.101145

Figure 1. Sample preparation of XFC-cycled graphite electrode #1 (9C, 450 cycles) for NeXT imaging
(A) Optical image of the graphite electrode containing Li deposits.[24] A ~1 mm wide graphite strip was cut around the cyan dotted rectangle.
(B) The strip was sealed inside a 1.5 mm diameter glass capillary, which was supported by a polyimide tube outside the imaging area for NeXT.
(C) Schematic illustration of NeXT setup located at the BT-2 imaging beamline at the National Institute of Standards and Technology Center for Neutron Research.[25]
(A) was adapted with permission from Paul et al.[24] Copyright 2021 American Chemical Society.

In this work, we first demonstrate the value of simultaneous neutron- and X-ray-based tomography (NeXT) as a non-destructive imaging modality for *ex situ* three-dimensional (3D) visualization of degradation on graphite electrodes cycled under extreme fast charging (XFC) (Figure 1). Second, we establish the benefits of the simultaneous nature of NeXT for battery characterization by combining the neutron and X-ray μCT data from the same battery location in 2D bivariate histogram phase segmentation. Specifically, we show characterization of one pristine and two XFC-cycled graphite electrode strips (9C charging for 450 cycles). We discuss the database-derived neutron and X-ray linear attenuation coefficients that serve as the basis of materials identification in the 2D segmentations. Our *ex situ* analysis motivates the design of NeXT-friendly LIB geometries for *in situ* and/or operando visualization of electrode degradation at the separator-electrolyte-electrode interface during XFC. For *in situ* NeXT-friendly cell design, particular attention needs to be paid to the casing materials, metal shims, and pistons from both neutron[15–18] and X-ray imaging[19–23] perspectives.

RESULTS

NeXT imaging of pristine and XFC-cycled graphite electrodes
In this section, we analyze the 2D grayscale neutron and X-ray images of the pristine and XFC-cycled graphite electrodes. Using the total neutron linear attenuation coefficients, μ_{n_tot}, at a 0.18 nm neutron wavelength and total X-ray linear attenuation coefficients, μ_{X_tot}, at 26.9 keV X-ray energy, from the standard neutron and X-ray material databases,[9,26,27] we explain our findings (Tables S1 and S2). Detailed calculations are given in Data S1. Together, our results highlight the advantage of combining neutron and X-ray data to bring out the strength of each method.

Figure 2 shows the reconstructed and registered 2D neutron and X-ray images of the pristine and XFC-cycled graphite electrodes. Our neutron imaging data show that graphite is indistinguishable from the Cu current collector (CC) in the pristine electrode (Figure 2A, cyan ellipse), whereas the corresponding X-ray images noticeably show Cu (Figure 2A, yellow ellipse). For the cycled electrodes, graphite is clearly visible in the neutron images (Figure 2B, cyan ellipses) and distinguishable from the CC only because they are physically separated from each other. However, the graphite is not clearly visible across all X-ray slices shown, although it can be seen very faintly in the X-ray slices when it is physically separated from Cu (Figure 2B, orange ellipse). Here, slice denotes the 2D projections of the 3D volume obtained
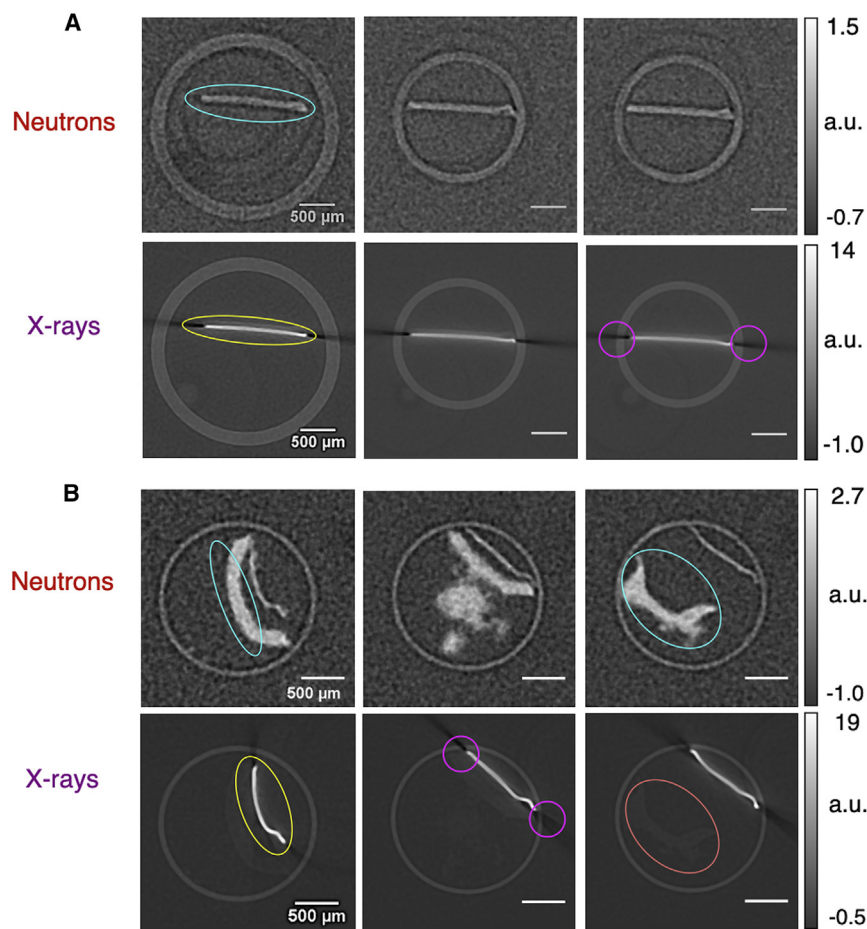
CellPress
OPEN ACCESS

Figure 2. 2D grayscale neutron and X-ray slices of 3D volume taken along the length of the electrode strip (z direction) from top to bottom

(A) Pristine and (B) XFC-cycled graphite electrode (9C for 450 cycles). The decreasing diameter and thickness of the outer glass capillary in the images from left to right in (A) is due to its funnel-like geometry. The grayscale bar on the right has arbitrary units (a.u.) and was created using 32 bit images in ImageJ.

along the length of the cut electrode strip. All the neutron and X-ray images reveal the outer glass capillary (silica) that housed the electrode strips in Figure 2. Additionally, our X-ray imaging data show beam-hardening artifacts due to the strongly attenuating Cu, which appear as dark streaks around the edges of Cu in both pristine and cycled electrodes (Note S1; Figures S1A1 and S1B1, red circles). To reduce these artifacts, we used an iterative physics-based beam-hardening correction in the LTT software for metal artifact reduction (MAR).[28] Although the MAR-corrected data reduced artifacts, some dark streaks persisted due to missing projections in μCT data when Cu was parallel to the X-ray beam, as can be seen in Figures 2 (pink circles) and S1A2 and S1B2 (red circles).

We note that the XFC-cycled electrode delaminated from the Cu CC, which was likely exacerbated during sample preparation as seen in Figure 2B. We believe that the varying electrode morphology is a result of the formation of the plated Li from extended XFC cycling at 9 C-rate for 450 cycles, which we have previously confirmed with X-ray diffraction (XRD).[29–31] In the present study, the plated Li was exposed to moisture during the pouch disassembly and/or subsequent sample

handling and converted into lithium hydroxide (LiOH) as per Equation 1 and confirmed by our XRD measurement (Note S2; Figure S2).

$$2Li_{(s)} + 2H_2O \rightarrow 2LiOH_{(s)} + H_{2(g)} \qquad \text{(Equation 1)}$$
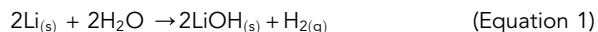
We explain these imaging results using μ_{n_tot} and μ_{X_tot}. In accordance with our imaging results, Cu with a μ_{X_tot} of $\sim$133 cm^{-1}, which is >200 times than both graphite and LiOH, should be clearly visible with X-rays in contrast to graphite and LiOH, which will be difficult to distinguish. Moreover, due to the sensitivity of neutrons to LiOH ($\mu_{n_tot_LiOH}$ = 5.82 cm^{-1}), regions of the XFC-cycled electrode that contain LiOH are clearly visible in neutron images. In addition, since $\mu_{n\_tot\_LiOH}$ is $\sim$5 times greater than $\mu_{n\_tot\_Cu}$, neutron µCT holds promise for imaging plated Li species. However, the low relative neutron contrast between Cu and graphite ($\mu_{n\_tot\_Cu} : \mu_{n\_tot\_graphite} \sim 2$) made it impossible for us to distinguish them from each other in the neutron images.

Considering our NeXT analysis, we conclude that combining neutron and X-ray µCT data is advantageous since it provides a significantly enhanced ability to differentiate electrode components by making use of distinct attenuation coefficients in at least one imaging modality for all battery materials. Imaging simultaneously is beneficial because data are collected from the same sample location, making image registration easier and enabling easier identification of material phases than is possible in individual neutron and X-ray segmentations in CI.

2D grayscale to colorized segmented images of pristine and XFC-cycled graphite electrodes

Herein, we present segmentation of the pristine and XFC-cycled graphite electrodes' reconstructed volumes. Details of the conversion of dual-tomography grayscale imaging data to colorized segmented images using the 2D bivariate histogram phase segmentation[32] are outlined in Note S3.

Figure 3 shows the segmentation of the pristine graphite electrode. For the 2D histogram, we only used the top 200 slices and masked out the glass capillary in the physical space because the pristine electrode was very uniform. Since the 3D structure of the pristine electrode is not expected to change along the length of its strip, the slices used for analysis are representative of the full 3D volume.

For phase segmentation, we assigned the negative gray-level values and those around zero as the background (Figure 3C). The negative values in both the neutron and X-ray histograms are not physical and are related to statistical noise and experimental error in the reconstruction. We observe that the background peaks in the individual neutron and X-ray histograms are not symmetric. Although the background peak in the neutron histogram is centered around zero (Figure 3A), the peak in the corresponding X-ray histogram is centered roughly around 0.7 a.u. (Figure 3B). This slight peak shift in the X-ray histogram is not unexpected and is likely due to the X-ray beam-hardening artifacts around Cu and the background pixels that were removed while cropping the slices in ImageJ.

From the remaining two peaks in the bivariate histogram (Figure 3C), the peak corresponding to the lower X-ray gray-level values ($\sim$2.5 a.u.) was assigned to graphite since its database-derived linear X-ray attenuation coefficient is much smaller than that of Cu (Table S1). Note that the drawn boxes in Figure 3C refer to the entire area of the 2D peak that was assigned to the segmented material. Finally, we assigned the remaining peak in the bivariate histogram at the neutron gray-level value of $\sim$0.6 a.u. and an X-ray gray-level value of $\sim$9 a.u. to the Cu CC.
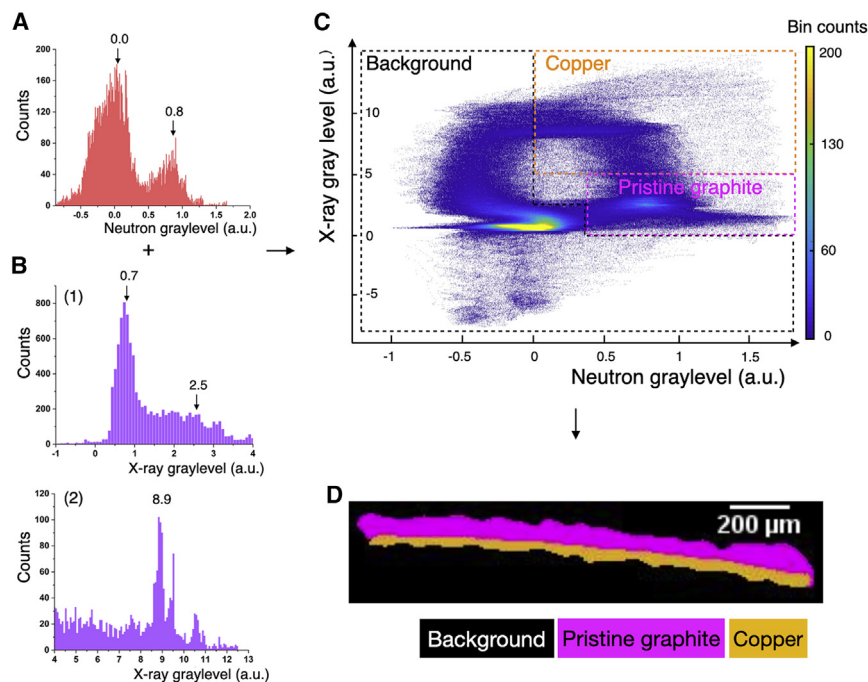
CellPress
OPEN ACCESS

Figure 3. 2D segmentation of the pristine graphite electrode

(A–C) Neutron (A), X-ray (B1 and B2), and 2D (C) bivariate histogram of the pristine electrode. Arrows in (A) and (B) point toward peaks corresponding to different material phases. (B1) and (B2) represent X-ray histograms across two different X-ray gray-level regions with different vertical axes to clearly show background, pristine graphite, and Cu peaks.

(D) Colorized segmented image showing graphite and Cu CC located spatially next to each other as expected.

To assess the quality of our phase segmentation (Note S3; Figure S3), we examined the 2D slice of the segmented volume of the pristine electrode (Figure 3D). The segmented slice shows that both graphite and Cu CC are adjacent to each other as expected. In addition, the width of the strip is ~1.4 mm (nominal width ~1.5 mm as measured by rule prior to cutting). The mean experimental graphite thickness is 69 ± 9 μm (nominal thickness = 70 μm), and the mean experimental Cu thickness is 35 ± 7 μm (nominal thickness = 10 μm). To calculate the experimental thicknesses, we averaged 20–30 measured locations. Considering the resolution of the NeXT setup (15–20 μm) and the strong X-ray attenuation of Cu, the overestimation of the Cu CC thickness is not surprising.[33,34]

Figure 4 shows the segmentation of XFC-cycled graphite electrode #1. We have provided segmentation results of XFC-cycled electrode #2 in Note S4 and Figures S4–S7 and detail only electrode #1 here because the two segmentations are consistent. This consistency between different electrodes provides confidence in our conclusions. For the 2D histogram, we masked out the glass capillary in the physical space. In addition, we first assigned all negative gray-level values and those around zero to the background (Figure 4C). Next, we assigned the peak at the neutron gray-level value of ~2.2 a.u. and an X-ray gray-level value of ~0.3 a.u. to the cycled graphite since the database-derived linear X-ray attenuation coefficient of graphite is much lower than that of Cu (Figure S8; Table S1). Because the cycled graphite delaminated from the Cu CC, X-ray beam-hardening artifacts from Cu, and hence their effect on the X-ray gray-level value of cycled graphite, were minimized. The presence of highly
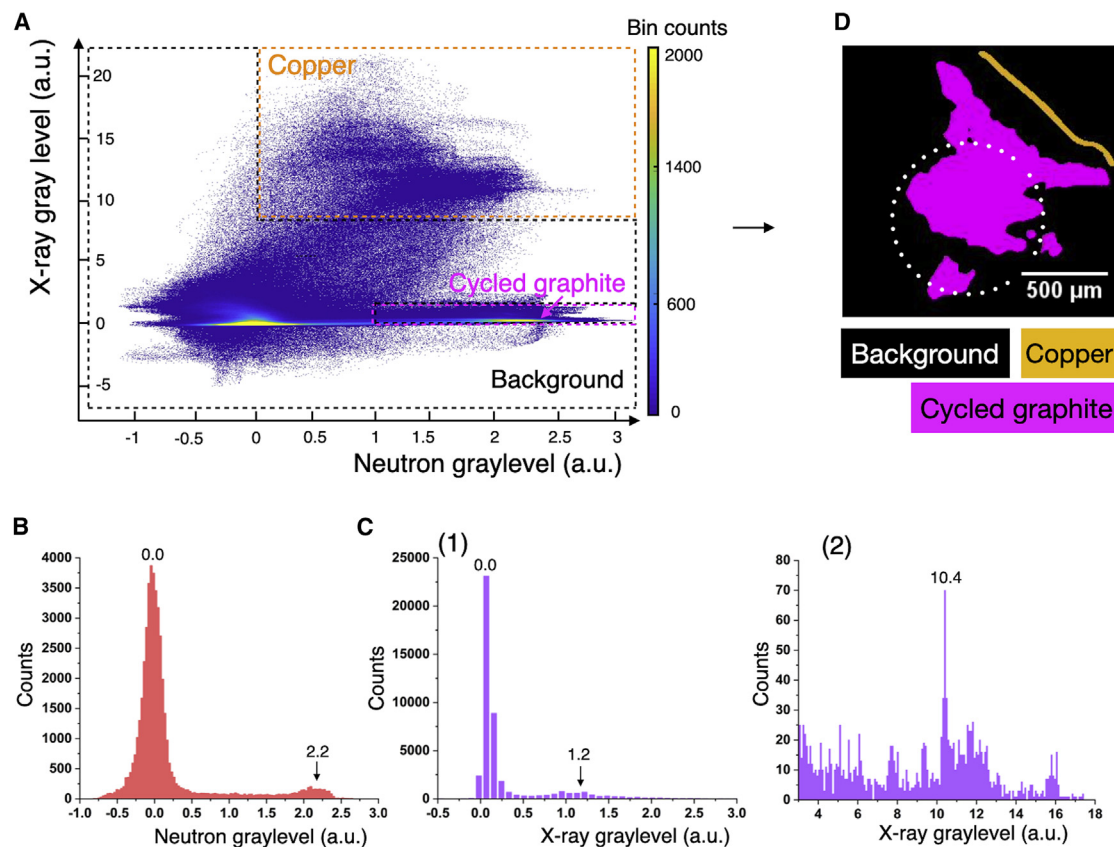
Figure 4. 2D segmentation of XFC-cycled graphite electrode #1 (containing LiOH)

(A) 2D bivariate histogram.

(B) Individual neutron.

(C1 and C2) X-ray histograms of cycled graphite electrode #1 at 9C, 450 cycles. (C1) and (C2) represent X-ray histograms across two different X-ray gray-level regions with different vertical axes to clearly show background, cycled graphite, and Cu peaks.

(D) 2D colorized segmented image of the cycled electrode, showing LiOH-containing protrusion (white dotted circle).

neutron-attenuating LiOH in the cycled electrode contributed to the higher neutron gray-level value of cycled graphite. However, we could not segment LiOH from the cycled graphite, which we believe is most likely due to the porosity in LiOH. Since pores are below the NeXT spatial resolution limit of ~15–20 μm and they decrease the average density and neutron gray-level value of LiOH, the observed relative neutron contrast between LiOH and cycled graphite was too small for segmentation.

Next, we assigned the peak at the neutron gray-level value of ~1.4 a.u. and an X-ray gray-level value of ~10 a.u. to the Cu CC. Lastly, any remaining few voxels between the Cu and cycled graphite peaks were assigned as background because they spatially belonged to the open space in the sample. Our measured thickness of the segmented Cu (35 ± 4 μm) in cycled electrode #1 matches well with the Cu thickness in the pristine electrode (35 ± 7 μm). Additionally, Tables S3 and S4 show consistency of observed neutron and X-ray gray-level values and Cu thicknesses of the pristine and two XFC-cycled graphite electrodes.

Figure S9 compares the 3D segmented volume of the pristine electrode (Figure S9A) with that of the XFC-cycled electrode (Figure S9B). We observe growth of the

CellPress
OPEN ACCESS

LiOH-containing protrusion visible in the 3D-segmented volume of XFC-cycled electrode #1, which can be correlated with the white Li deposits on the optical image of the electrode (Figure S9, left). For example, the lines labeled c and d on the 3D visualization and 2D segmented slices in Figure S9B (left) correspond to the thick yellow lines labeled c and d on the optical image in Figure S9B (right). Our previous studies[8,29–31] on mm-scale spatial XRD maps of the cycled electrode show that the white deposits in the optical image correspond to irreversibly plated Li containing trapped lithiated graphite (LiC_6 and LiC_{12}) underneath (Note S5; Figure S10). Since the total volume expansion of a fully lithiated LiC_6 is approximately 13%[35] and the amount of lithiated graphite relative to irreversibly plated Li in the electrode's discharged state is small, we rely on the following assumptions to interpret our results: (1) all the irreversibly plated Li converted into LiOH, and (2) LiOH is hygroscopic and porous. With these assumptions, the plated Li will convert to LiOH and undergo significant volume expansion, and the morphology of the cycled electrode will vary along the strip length due to differing amounts of plated Li. In addition, the delamination of the XFC-cycled graphite from the Cu CC visualized in Figures S9B and S7 is likely due to the more fragile nature of the two cycled electrodes (compared with the pristine), which was exacerbated during sample preparation.

Our imaging results reveal NeXT potential for *ex situ* 3D visualization of graphite electrode degradation. Imaging graphite electrode degradation during operando and/or *in situ* battery cycling can help reveal the onset and rate of progression of electrode degradation in real time, hence advancing our mechanistic understanding of LIB failure during XFC. However, to fully utilize the unique advantages of combining neutron and X-ray μCT data, design of a NeXT-friendly LIB is needed.[36]

DISCUSSION

This work demonstrates the feasibility of NeXT as a non-destructive characterization method for *ex situ* 3D visualization of graphite electrode degradation following XFC. Our results highlight the primary advantage of NeXT for LIB research: combining the strength of each imaging modality by overlapping neutron and X-ray data from the same sample location for material identification. The segmented images of the XFC-cycled graphite electrodes show a qualitative correlation between electrode degradation and the presence of plated Li protrusions. Based on our XRD data, we explain these protrusions by the formation of LiOH and/or possibly its hydrated porous crystallites because of Li exposure to moisture during sample preparation. In the absence of moisture and other sample preparation effects, the degradation effects are expected to be Li deposits and possibly some delamination from the Cu CC.[24,29,37] Finally, our *ex situ* methodology development can be utilized to investigate fundamental research questions by other battery chemistries[38] such as (1) Li-O_2 batteries that cycle via LiOH formation and decomposition;[39] (2) Li-metal batteries that plate and strip plated Li;[40] (3) solid-state Li-S batteries;[41] (4) Li-iodine cells;[42] and (5) Li-Si cells.[43] Future work involves designing a NeXT-friendly battery for operando and/or *in situ* observation of electrode degradation at the separator-electrolyte-electrode interface during XFC.

EXPERIMENTAL PROCEDURES

Resource availability

Lead contact

Further information and requests for resources and reagents should be directed to and will be fulfilled by the lead contact, Johanna Nelson Weker (jlnelson@slac.stanford.edu).

CellPress
OPEN ACCESS

Cell Reports
Physical Science
Report

Materials availability
This study did not generate new unique materials.

Data and code availability
The authors declare that the data supporting the findings of this study are available within the article and the supplemental information. Any additional information required to reanalyze the data reported in this paper is available from the lead contact upon request.

Sample preparation

The single-layer graphite/NMC532 pouch cells were assembled in a dry room environment at Argonne National Laboratory (ANL). Then, the pouch cells underwent formation cycling and degassing to be shipped to Idaho National Laboratory for XFC cycling at 9C charging and C/2 discharging for 450 cycles. Following XFC, cells was discharged to 3.0 V at C/2 followed by a 2 h voltage hold at 3.0 V to be shipped back to ANL for disassembly in a dry room. Then, the cycled graphite electrodes were harvested and soaked in dimethylformamide for around 2 min to wash away any residual electrolyte. The harvested electrodes were cut into rectangular pieces (1–2 mm in width and ∼30 mm in length) using ceramic scissors to allow full-field tomographic imaging. The pristine strip did not undergo any electrochemical cycling. Next, the electrode strips were sealed using epoxy inside the 1.5 mm diameter glass capillary in an Ar-filled glovebox. Between the cell disassembly and shipping for NeXT, Li was unintentionally exposed to moisture in the air, possibly from a slightly incomplete seal or during handling in the dry room, and transformed into LiOH, as confirmed by XRD using beamline 11-ID-B at the Advanced Photon Source (Figure S2). The XRD measurements were performed approximately 3 days after sample preparation and before shipping the samples for imaging. Also, the strip geometry may not be optimal for tomography, and hence other geometries (e.g., small disk shaped) should be considered. Further details of the sample preparation are outlined in the supplemental experimental procedures.

Simultaneous neutron and X-ray tomography

We performed NeXT at the BT-2 imaging beamline (Figure 1C) at the National Institute of Standards and Technology Center for Neutron Research.[25] Taking the neutron detector's response into consideration, the thermal neutron spectrum is centered around a wavelength of 0.18 nm with a Maxwellian distribution. The X-ray spectrum is centered around an energy of 27 keV. The as-reconstructed neutron and X-ray pixel sizes were ∼6.5 μm. The effective NeXT spatial resolution was ∼15–20 μm for a field of view of ∼1.65 × 1.7 cm. Further experimental details about NeXT are tabulated in Table S5. Notes S6 and S7 outline the NeXT image processing steps, along with Figures S11–S13. Table S6 lists the symbols alongside their definitions used in this manuscript.

SUPPLEMENTAL INFORMATION

Supplemental information can be found online at https://doi.org/10.1016/j.xcrp.2022.101145.

ACKNOWLEDGMENTS

Cell Reports
Physical Science
Report

AUTHOR CONTRIBUTIONS

M.Y., P.P.P., J.N.W., and J.M.L. performed NeXT experiments. M.Y. and J.M.L. developed the image processing framework. P.P.P. and C.C. conducted the XRD measurements. A.R.D., A.N.J., B.J.P., and S.E.T. assembled and formed the LIB pouch cells. T.R.T. and E.J.D. XFC cycled the cells. M.Y., J.M.L., P.P.P., D.N.A.-B., C.C., A.R.D., A.N.J., B.J.P., S.E.T., T.R.T., E.J.D., V.T., H.-G.S., M.F.T., and J.N.W. discussed the experimental results and reviewed the paper. The manuscript was written through contributions of all authors. All authors have approved the final version of the manuscript.

DECLARATION OF INTERESTS

The authors declare no competing interests.

INCLUSION AND DIVERSITY

One or more of the authors of this paper self-identifies as an underrepresented ethnic minority in their field of research or within their geographical location. One or more of the authors of this paper self-identifies as a gender minority in their field of research. One or more authors of this paper received support from a program designed to increase minority representation in their field of research. While citing references scientifically relevant for this work, we also actively worked to promote gender balance in our reference list.

REFERENCES

1. Pietsch, P., and Wood, V. (2017). X-ray tomography for lithium-ion battery research: a practical guide. Annu. Rev. Mater. Res. 47, 451–479.

2. Müller, S., Pietsch, P., Brandt, B.E., Baade, P., De Andrade, V., De Carlo, F., and Wood, V. (2018). Quantification and modeling of mechanical degradation in lithium-ion batteries based on nanoscale imaging. Nat. Commun. 9, 2340. https://doi.org/10.1038/s41467-018-04477-1.

3. Han, X., Lu, L., Zheng, Y., Feng, X., Li, Z., Li, J., and Ouyang, M. (2019). A review on the key issues of the lithium-ion battery degradation among the whole life cycle. ETransportation 1, 100005. https://doi.org/10.1016/j.etran.2019.100005.

4. Liu, Y., Zhu, Y., and Cui, Y. (2019). Challenges and opportunities towards fast-charging battery materials. Nat. Energy 4, 540–550. https://doi.org/10.1038/s41560-019-0405-3.

5. Ziesche, R.F., Kardjilov, N., Kockelmann, W., Brett, D.J., and Shearing, P.R. (2022). Neutron imaging of lithium batteries. Joule 6, 35–52. https://doi.org/10.1016/j.joule.2021.12.007.

6. Yang, H., Tang, P., Piao, N., Li, J., Shan, X., Tai, K., Tan, J., Cheng, H.M., and Li, F. (2022). In-situ imaging techniques for advanced battery development. Mater. Today 57, 279–294. https://doi.org/10.1016/j.mattod.2022.05.021.

CellPress OPEN ACCESS

Cell Reports Physical Science

Report

7. Atkins, D., Capria, E., Edström, K., Famprikis, T., Grimaud, A., Jacquet, Q., Johnson, M., Matic, A., Norby, P., Reichert, H., et al. (2022). Accelerating battery characterization using neutron and Synchrotron techniques: toward a multi-modal and multi-scale standardized experimental workflow. Adv. Energy Mater. 12, 2102694. https://doi.org/10.1002/aenm.202102694.

8. Paul, P.P., McShane, E.J., Colclasure, A.M., Balsara, N., Brown, D.E., Cao, C., Chen, B., Chinnam, P.R., Cui, Y., Dufek, E.J., et al. (2021). A review of existing and emerging methods for lithium detection and characterization in Li-ion and Li-metal batteries. Adv. Energy Mater. 11, 2100372. https://doi.org/10.1002/aenm.202100372.

9. https://www.nist.gov/ncnr/neutron-scattering-lengths-list.

10. Ziesche, R.F., Arlt, T., Finegan, D.P., Heenan, T.M.M., Tengattini, A., Baum, D., Kardjilov, N., Markötter, H., Manke, I., Kockelmann, W., et al. (2020). 4D imaging of lithium-batteries using correlative neutron and X-ray tomography with a virtual unrolling technique. Nat. Commun. 11, 777. https://doi.org/10.1038/s41467-019-13943-3.

11. Ziesche, R.F., Robinson, J.B., Kok, M.D.R., Markötter, H., Kockelmann, W., Kardjilov, N., Manke, I., Brett, D.J.L., and Shearing, P.R. (2020). Editors' choice—4D neutron and x-ray tomography studies of high energy density primary batteries: part I. Dynamic studies of LiSOCl2 during discharge. J. Electrochem. Soc. 167, 130545. https://iopscience.iop.org/article/10.1149/1945-7111/abbbbc/meta.

12. Sun, F., Gao, R., Zhou, D., Osenberg, M., Dong, K., Kardjilov, N., Hilger, A., Markötter, H., Bieker, P.M., Liu, X., and Manke, I. (2018). Revealing hidden facts of Li anode in cycled lithium–oxygen batteries through X-ray and neutron tomography. ACS Energy Lett. 4, 306–316. https://doi.org/10.1021/acsenergylett.8b02242.

13. LaManna, J., Chen, J.H., Althaus, S., Liu, Y., Hussey, D., and Jacobson, D. (2020). Bivariate histogram segmentation of simultaneous neutron and X-ray tomography for improved compositional and structural determination of Source rock shales. Microsc. Microanal. 26, 3220–3221. https://doi.org/10.1017/S1431927620024204.

14. Kaestner, A.P., Hovind, J., Boillat, P., Muehlebach, C., Carminati, C., Zarebanadkouki, M., and Lehmann, E.H. (2017). Bimodal imaging at ICON using neutrons and X-rays. Physics Procedia 88, 314–321. https://doi.org/10.1016/j.phpro.2017.06.043.

15. Pang, W.K., and Peterson, V.K. (2015). A custom battery for operando neutron powder diffraction studies of electrode structure. J. Appl. Crystallogr. 48, 280–290. https://doi.org/10.1107/S1600576715000679.

16. Knoche, T., Zinth, V., Schulz, M., Schnell, J., Gilles, R., and Reinhart, G. (2016). In situ visualization of the electrolyte solvent filling process by neutron radiography. J. Power Sources 331, 267–276. https://doi.org/10.1016/j.jpowsour.2016.09.037.

17. Sun, F., Markötter, H., Manke, I., Hilger, A., Alrwashdeh, S.S., Kardjilov, N., and Banhart, J. (2017). Complementary X-ray and neutron radiography study of the initial lithiation process in lithium-ion batteries containing silicon electrodes. Appl. Surf. Sci. 399, 359–366. https://doi.org/10.1016/j.apsusc.2016.12.093.

18. Campillo-Robles, J.M., Goonetilleke, D., Soler, D., Sharma, N., Martín Rodríguez, D., Bücherl, T., Makowska, M., Türkilmaz, P., and Karahan, V. (2019). Monitoring lead-acid battery function using operando neutron radiography. J. Power Sources 438, 226976.

19. Borkiewicz, O.J., Wiaderek, K.M., Chupas, P.J., and Chapman, K.W. (2015). Best practices for operando battery experiments: influences of X-ray experiment design on observed electrochemical reactivity. J. Phys. Chem. Lett. 6, 2081–2085. https://doi.org/10.1016/j.jpowsour.2019.226976.

20. Jervis, R., Brown, L.D., Neville, T.P., Millichamp, J., Finegan, D.P., Heenan, T.M.M., Brett, D.J.L., and Shearing, P.R. (2016). Design of a miniature flow cell for in situ x-ray imaging of redox flow batteries. J. Phys. D Appl. Phys. 49, 434002. https://doi.org/10.1088/0022-3727/49/43/434002.

21. Tan, C., Daemi, S.R., Taiwo, O.O., Heenan, T.M.M., Brett, D.J.L., and Shearing, P.R. (2018). Evolution of electrochemical cell designs for in-situ and operando 3D characterization. Materials 11, 2157. https://doi.org/10.3390/ma11112157.

22. Finegan, D.P., Quinn, A., Wragg, D.S., Colclasure, A.M., Lu, X., Tan, C., Heenan, T.M.M., Jervis, R., Brett, D.J.L., Das, S., et al. (2020). Spatial dynamics of lithiation and lithium plating during high-rate operation of graphite electrodes. Energy Environ. Sci. 13, 2570–2584. https://doi.org/10.1039/D0EE01191F.

23. Cao, C., Steinrück, H.G., Paul, P.P., Dunlop, A.R., Trask, S.E., Jansen, A.N., Kasse, R.M., Thampy, V., Yusuf, M., Weker, J.N., et al. (2022). Conformal pressure and fast-charging Li-ion batteries. J. Electrochem. Soc. 169, 040540. https://doi.org/10.1149/1945-7111/ac653f.

24. Paul, P.P., Cao, C., Thampy, V., Steinrück, H.G., Tanim, T.R., Dunlop, A.R., et al. (2021). Using in situ high-energy X-ray diffraction to quantify electrode behavior of Li-ion batteries from extreme fast charging. 4, https://pubs.acs.org/doi/10.1021/acsaem.1c02348.

25. LaManna, J., Hussey, D., Baltic, E., and Jacobson, D. (2017). Neutron and X-ray Tomography (NeXT) system for simultaneous, dual modality tomography. Review of Scientific Instruments 88, 113702. https://doi.org/10.1063/1.4989642.

26. https://www.ncnr.nist.gov/resources/activation/.

27. https://physics.nist.gov/PhysRefData/Xcom/html/xcom1.html.

28. Champley, K.M., Willey, T.M., Kim, H., Bond, K., Glenn, S.M., Smith, J.A., Kallman, J.S., Brown, W.D., Seetho, I.M., Keene, L., et al. (2022). Livermore tomography tools: accurate, fast, and flexible software for tomographic science. NDT E Int. 126, 102595. https://doi.org/10.1016/j.ndteint.2021.102595.

29. Paul, P.P., Thampy, V., Cao, C., Steinrück, H.G., Tanim, T.R., Dunlop, A.R., Dufek, E.J., Trask, S.E., Jansen, A.N., Toney, M.F., and Nelson Weker, J. (2021). Quantification of heterogeneous, irreversible lithium plating in extreme fast charging of lithium-ion batteries. Energy Environ. Sci. 14, 4979–4988. https://doi.org/10.1039/D1EE01216A.

30. Tanim, T.R., Dufek, E.J., Evans, M., Dickerson, C., Jansen, A.N., Polzin, B.J., Dunlop, A.R., Trask, S.E., Jackman, R., Bloom, I., et al. (2019). Extreme fast charge challenges for lithium-ion battery: variability and positive electrode issues. J. Electrochem. Soc. 166, A1926–A1938. https://iopscience.iop.org/article/10.1149/2.0731910jes/meta.

31. Tanim, T.R., Dufek, E.J., Dickerson, C.C., and Wood, S.M. (2019). Electrochemical quantification of lithium plating: challenges and considerations. J. Electrochem. Soc. 166, A2689–A2696. https://iopscience.iop.org/article/10.1149/2.1581912jes/meta.

32. LaManna, J.M., Hussey, D.S., DiStefano, V.H., Baltic, E., and Jacobson, D.L. (2020). NIST NeXT: a system for truly simultaneous neutron and x-ray tomography. In Hard X-Ray, Gamma-Ray, and Neutron Detector Physics XXII, 11494, A. Burger, S.A. Payne, and M. Fiederle, eds., Hard X-Ray, Gamma-Ray, and Neutron Detector Physics XXII (International Society for Optics and Photonics), p. 114940P.

33. Ketcham, R.A., and Mote, A.S. (2019). Accurate measurement of small features in X-ray CT data volumes, demonstrated using gold grains. J. Geophys. Res. Solid Earth 124, 3508–3529. https://doi.org/10.1029/2018JB017083.

34. Do, S., Karl, W.C., Liang, Z., Kalra, M., Brady, T.J., and Pien, H.H. (2011). A decomposition-based CT reconstruction formulation for reducing blooming artifacts. Phys. Med. Biol. 56, 7109–7125. https://iopscience.iop.org/article/10.1088/0031-9155/56/22/008/meta.

35. Schweidler, S., de Biasi, L., Schiele, A., Hartmann, P., Brezesinski, T., and Janek, J. (2018). Volume changes of graphite anodes revisited: a combined operando X-ray diffraction and in situ pressure analysis study. J. Phys. Chem. C 122, 8829–8835. https://doi.org/10.1021/acs.jpcc.8b01873.

36. Yusuf, M., LaManna, J.M., Preefer, M., Paul, P.P., Agyeman-Budu, D.N., Toney, M.F., and Nelson Weker, J. (2021). Design and characterization of a neutron-friendly lithium-ion battery coin cell for extreme fast-charging. In ECS Meeting Abstracts, 4ECS Meeting Abstracts (IOP Publishing), p. 441. https://iopscience.iop.org/article/10.1149/MA2021-024441mtgabs/meta.

37. Tanim, T.R., Paul, P.P., Thampy, V., Cao, C., Steinrück, H.G., Nelson Weker, J., Toney, M.F., Dufek, E.J., Evans, M.C., Jansen, A.N., et al. (2020). Heterogeneous behavior of lithium plating during extreme fast charging. Cell Rep. Phys. Sci. 1, 100114. https://doi.org/10.1016/j.xcrp.2020.100114.

38. Ziesche, R.F., Kardjilov, N., Kockelmann, W., Brett, D.J., and Shearing, P.R. (2022). Neutron imaging of lithium batteries. Joule 6, 35–52. https://doi.org/10.1016/j.joule.2021.12.007.

Cell Reports
Physical Science
Report

CellPress
OPEN ACCESS

39. Liu, T., Leskes, M., Yu, W., Moore, A.J., Zhou, L., Bayley, P.M., Kim, G., and Grey, C.P. (2015). Cycling Li-O2 batteries via LiOH formation and decomposition. Science *350*, 530–533. https://doi.org/10.1126/science.aac7730.

40. Geise, N.R., Kasse, R.M., Nelson Weker, J., Steinrück, H.G., and Toney, M.F. (2021). Quantification of efficiency in lithium metal negative electrodes via operando X-ray diffraction. Chem. Mater. *33*, 7537–7545. https://doi.org/10.1021/acs.chemmater.1c02585.

41. Bradbury, R., Dewald, G.F., Kraft, M.A., Arlt, T., Kardjilov, N., Janek, J., and Ohno, S. (2021). Visualizing Reaction Fronts and Transport Limitations in Solid-State Li-S Batteries via Operando Neutron Imaging. Preprint at ChenRxiv. https://doi.org/10.26434/chemrxiv-2021-vwnpt-v2.

42. Strobl, M., Manke, I., Kardjilov, N., Hilger, A., Dawson, M., and Banhart, J. (2009). Advances in neutron radiography and tomography. J. Phys. D Appl. Phys. *42*, 243001. https://iopscience.iop.org/article/10.1088/0022-3727/42/24/243001/meta.

43. Sun, F., Markötter, H., Manke, I., Hilger, A., Alrwashdeh, S.S., Kardjilov, N., and Banhart, J. (2017). Complementary X-ray and neutron radiography study of the initial lithiation process in lithium-ion batteries containing silicon electrodes. Appl. Surf. Sci. *399*, 359–366. https://iopscience.iop.org/article/10.1088/0022-3727/42/24/243001/meta.